remote sensing

MDPI

Article

A Case Study of Polar Cap Sporadic-E Layer Associated with TEC Variations

Yong Wang [1,2], Periyadan T. Jayachandran [2], David R. Themens [2,3], Anthony M. McCaffrey [2], Qing-He Zhang [1,*], Shiva David [2] and Richard Chadwick [2]

1 Shandong Provincial Key Laboratory of Optical Astronomy and Solar-Terrestrial Environment, School of Space Science and Physics, Institute of Space Sciences, Shandong University, Weihai 264209, China; wangyong180@sdu.edu.cn

2 Physics Department, University of New Brunswick, Fredericton, NB E3B 5A3, Canada; jaya@unb.ca (P.T.J.); david.themens@unb.ca (D.R.T.); a.mccaffrey@unb.ca (A.M.M.); sdavid1@unb.ca (S.D.); rchadwic@unb.ca (R.C.)

3 Space Environment and Radio Engineering Group (SERENE), School of Engineering, University of Birmingham, Birmingham B15 2TT, UK

* Correspondence: zhangqinghe@sdu.edu.cn; Tel.: +86-631-5688126

Abstract: The Sporadic-E (Es) layer is an often-observed phenomenon at high latitudes; however, our understanding of the polar cap Es layer is severely limited due to the scarce number of measurements. Here, the first comprehensive study of the polar cap Es layer associated with Global Positioning System (GPS) Total Electron Content (TEC) variations and scintillations is presented with multiple measurements at Resolute, Canada (Canadian Advanced Digital Ionosonde (CADI), Northward-looking face of Resolute Incoherent-Scatter Radar (RISR-N), and GPS receiver). According to the joint observations, the polar cap Es layer is a thin patch structure with variously high electron density, which gradually develops into the lower E region (~100 km) and horizontally extends >200 km. Moreover, the TEC variations produced by the polar cap Es layer are pulse-like enhancements with a general amplitude of ~0.5 TECu and are followed by smaller but rapid TEC perturbations. Furthermore, the possible scintillation effects likely associated with the polar cap Es layer are also discussed. As a consequence, the results widely expand our understanding on the polar cap Es layer, in particular on TEC variations.

Keywords: polar cap; the sporadic-E layer; Resolute Bay; spatial structures; TEC variations; scintillations

Citation: Wang, Y.; Jayachandran, P.T.; Themens, D.R.; McCaffrey, A.M.; Zhang, Q.-H.; David, S.; Chadwick, R. A Case Study of Polar Cap Sporadic-E Layer Associated with TEC Variations. *Remote Sens.* **2021**, *13*, 1324. https://doi.org/10.3390/rs13071324

Received: 18 February 2021
Accepted: 27 March 2021
Published: 31 March 2021

1. Introduction

The Sporadic-E (Es) layer is normally a thin layer with quite variable peak density at an altitude range of 90−120 km and is predominately composed of metallic ions (such as Fe^+ and Mg^+) deposited by meteor ablation into the ionosphere [1–7]. These metallic ions have a longer lifetime than NO^+ and $O_2{}^+$ (the main ion species in the lower E region) due to a lower recombination rate; therefore, they can accumulate into a thin layer that can last several hours. The Es layer is produced by the compression of these ion populations through the complicated mechanisms of neutral winds and/or electric fields and/or gravity waves [3,4,8–11].

Referring to the formation mechanism of the Es layer at mid-latitudes, it is a widely accepted view that the vertical convergence of the metal ions is primarily driven by the wind shears [12–16]; however, at high latitudes the formation of the polar cap Es layer is not simply explained only by wind shears, as the almost vertical direction of magnetic field relegates this mechanism to a secondary formation source; as such, strong electric fields have been proposed as the dominate effect on drifting metallic ions [17,18]. This primary function has then been generally checked, suggesting that two necessary conditions should be satisfied to produce Es layers, namely: a magnetically westward electric field and an

abundance of metallic ions [17–20]. Meanwhile, gravity waves are also considered a more important factor than the neutral wind on the distribution of metallic ions [21–25]. Due to these complicated formation processes of the polar cap Es layer and also the limitation of observation measurements at high latitudes, measurements from more instruments are therefore urgently required to deeply understand this thin layer.

In recent decades, the characteristics of these thin layers have been generally investigated by using a series of instruments, incompletely including ionosondes, ground-based radars, radio-occultation techniques, as well as GPS receivers [9,16,22,26–31]; however, due to the spatial and temporal limitations of measurements of Es layers, there is much we do not understand about the Es layer, especially over the polar region, e.g., the horizontal scale, the formation mechanism, the corresponding GPS Total Electron Content (TEC) variations, as well as scintillations. Fortunately, Resolute provides a very good opportunity to extensively study the polar cap Es layer through joint observations of measurements, including a Canadian Advanced Digital Ionosonde (CADI), the northward-looking face of Resolute Incoherent-Scatter Radar (RISR-N), and a ground-based GPS receiver.

In this study, we will first detail the various specifications, advantages, and shortcomings of the involved instruments. Through the simultaneous measurements of the CADIs at Resolute Bay/Eureka/Pond Inlet and RISR-N, an interesting example of polar cap Es layer is then presented in detail, examining its vertical and horizontal scale. Moreover, benefiting from the combined data of the GPS receiver, the phenomena of TEC variations associated with the polar cap Es layer are firstly investigated. At last, the sections of discussions and conclusions are carried out.

2. Instruments and Data Sets

The Canadian High Arctic Ionospheric Network (CHAIN) currently consists of 9 CADIs and 25 GPS receivers distributed in the Canadian Arctic. In this paper, only four CADIs from CHAIN are involved, which are respectively sited at Eureka (EU, geographic: 79.99°N, 85.9°W; geomagnetic latitude: 87.87°N), Resolute Bay (RB, geographic: 74.73°N, 94.91°W; geomagnetic latitude: 82.43°N), Pond Inlet (PO, geographic: 72.69°N, 77.96°W; geomagnetic latitude: 81.30°N), and Cambridge Bay (CA, geographic: 69.10°N, 105.12°W; geomagnetic latitude: 77.02°N). The locations of these CADIs are specified in Figure 1a by yellow stars under the geographical latitude/longitude coordinate system. Note that three supportive CADIs from EU, PO, and CA are the nearest ground-based instruments around the RB. Two tracks of GPS Pseudo-Random Noise (PRN) 18 and GPS PRN19 (coded by the light and dark blue colors, respectively) were superimposed on the Ionospheric Pierce Point (IPP) at an altitude of 110 km during the conducted period.

Meanwhile, a number of instruments were deployed to Resolute Bay (RB) to simultaneously and comprehensively monitor the ionosphere over the central polar cap. In this study, only CHAIN CADI, RISR-N, and GPS receivers were examined. The relative positions of these instruments, as well as their viewing geometry, are shown in Figure 1b as a function of elevation and azimuth, in which the CADI and GPS receiver are highlighted by the black bold square in the center and the phased-array beams of RISR-N are marked by black crosses with each beam number. Note that the CADI is almost collocating with the beam 8 of RISR-N, both detecting along the vertical direction. Two GPS satellite tracks of GPS PRN19 (dark blue) and PRN18 (light blue) were simultaneously examined during the period of interest and are discussed in the next section.

The CADI instrument is run by CHAIN [32] and provides both ionograms (1-min time resolution; not shown here) and the virtual altitude of echoes reflected from the ionosphere at a number of fixed frequencies (e.g., 4 MHz) every 30 s. RISR-N is a phased array system that can deploy a large number of beams simultaneously (as shown in Figure 1b), offering multiple profiles of electron density (Ne), electron temperature (Te), ion temperature (Ti), and ion velocity (Vi) along each line-of-sight direction [33]. When RISR-N is operating with an Alternating Code (AC 16-30) mode, the instrument can provide high resolution measurements in the lower E region, which can be used to study Es layers. For this

particular period below the altitude of 120 km, its range and time resolutions are ~4 km and ~3 min, respectively. Taking advantage of the fixed pattern of multiple beams of RISR-N, it presents us with a unique opportunity to examine polar cap Es layers in 3-dimension. Moreover, the Novatel GSV4004B GPS receiver, also operated by CHAIN, provides raw phase and amplitudes sampled at 50 Hz and phase-levelled TEC at 1 Hz. The GPS TEC data we used are the slant relative TEC with elevation angles greater than 10°, which are sufficient to examine TEC variations.

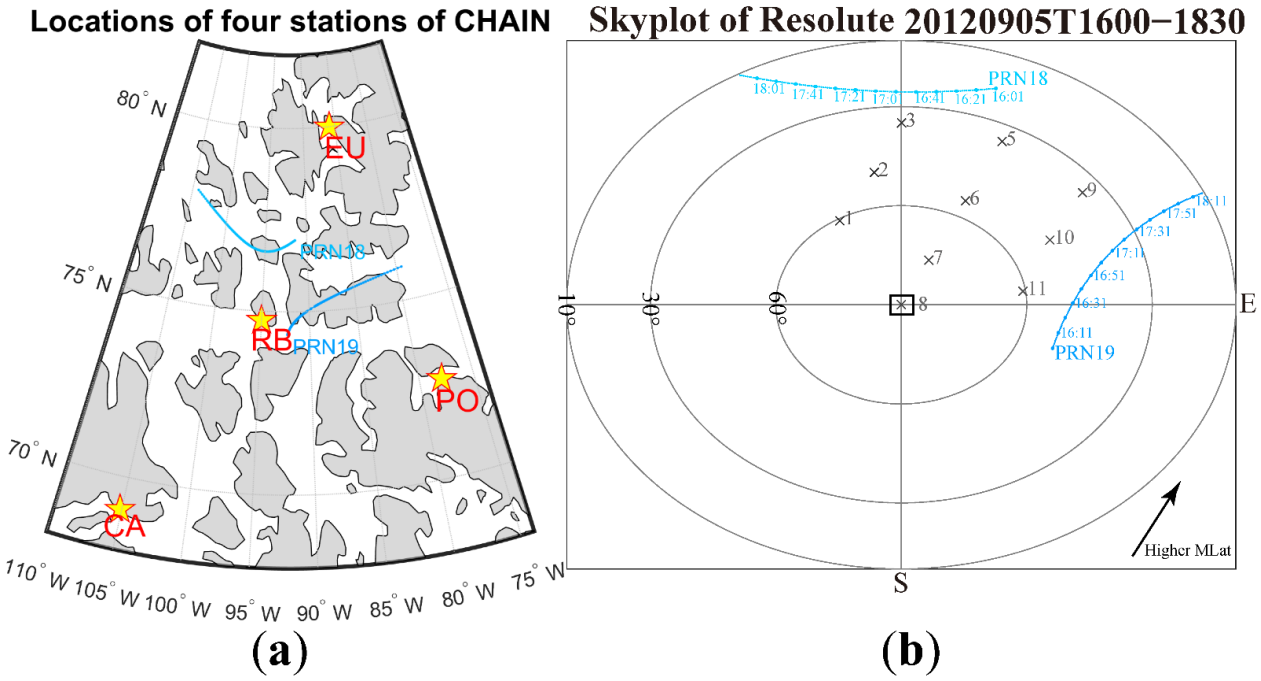

Figure 1. (**a**) The locations of four involved Canadian Advanced Digital Ionosonde (CADI) of the Canadian High Arctic Ionospheric Network (CHAIN) in the Canadian arctic marked by the yellow stars in geographic coordinate, at where EU stands for Eureka, RB for Resolute Bay, PO for Pond Inlet, and CA for Cambridge Bay. Simultaneously, two conducted GPS tracks of PRN18 (light blue) and PRN19 (dark blue) at the Ionospheric Pierce Point (IPP) altitude of 110 km in relation to RB were superimposed during a period of 16:00–18:30 UT on 5 September 2012; (**b**) the location of adopted instruments at RB as a function of elevation and azimuth, including CADI (the black square in the center), GPS receiver (sharing the same location with CADI), and the phased-array beams of the north incoherent scatter radar (RISR-N, the black crosses with a number). The black concentric circles respectively represent the elevations of 10° and 30° and 60°. Within the interested period, two ray paths of GPS PRN18 (light blue) and GPS PRN19 (dark blue) are marked by closed dots with Universal Time (UT), highlighting the change of locations to the observation instruments. The black arrow in the right-bottom corner is pointing to the higher magnetic latitude (MLat) for the period of interest.

In this paper, the data provided by the CADI and GPS receiver were all collected from CHAIN (ftp://chain.physics.unb.ca/gps/data/raw/resc/2012/09/ (accessed on 18 February 2021)), which is run by researchers in the Physics Department of University of New Brunswick (UNB). The RISR-N data were obtained from the Madrigal online database (http://cedar.openmadrigal.org/listExperiments?isGlobal=on&categories=1&instruments=91&showDefault=on&start_date_0=2012-01-01&start_date_1=00%3A00%3A00&end_date_0=2012-12-31&end_date_1=23%3A59%3A59 (accessed on 18 February 2021)), which was established by the Haystack Observatory of Massachusetts Institute of Technology (MIT).

3. Results

In this study, a number of experiments corresponding to the polar cap Es layer were collected since 2010, all including observations from these instruments at the RB simultane-

ously. As an example, a common experiment during the period of 16:00–21:00 Universal Time (UT) on 5 September 2012 was presented to study the characteristics of polar cap Es layer and then investigate the corresponding TEC variations, as well as the scintillations of amplitude and phase.

3.1. Solar Wind and IMF Conditions and Geomagnetic Indices

During the period of 15:00–22:00 UT on 5 September 2012, Figure 2 presents the solar wind and Interplanetary Magnetic Field (IMF) conditions as well as the geomagnetic indices. Parameters are: (a) the Geocentric Solar Magnetic (GSM) Interplanetary Magnetic Field (IMF) components; (b) the solar wind velocity, V_{SW}, and the solar wind number density, N_P; (c) the solar wind dynamic pressure, PDyn; (d) the auroral electrojet (AE/AU/AL) indices; and (e) the SYM-H index. Accounting for the travel from nose of bow shock to the polar ionosphere, the IMF and solar wind data were delayed 7 min. The IMF and solar wind conditions were weak (Figure 2a–c), resulting in quiet and stable geomagnetic conditions (Figure 2e). During the period of interest (highlighted by two vertical dashed lines), the IMF By/Bz components were decreasing from weak positive to stable negative (above −5 nT) at ~18:00 UT; on the contrary, the Bx was increasing from weak negative to around 0 at ~18:00 UT. Meanwhile, the solar wind velocity slowed from ~500 km/s to 450 km/s but the number density enhanced from ~18:00 UT, giving an increased but still weak PDyn (~4 nPa). The AE/AL indices reached ±500 nT from quiet conditions after ~18:00 UT, probably suggesting the occurrence of a moderate substorm at nightside.

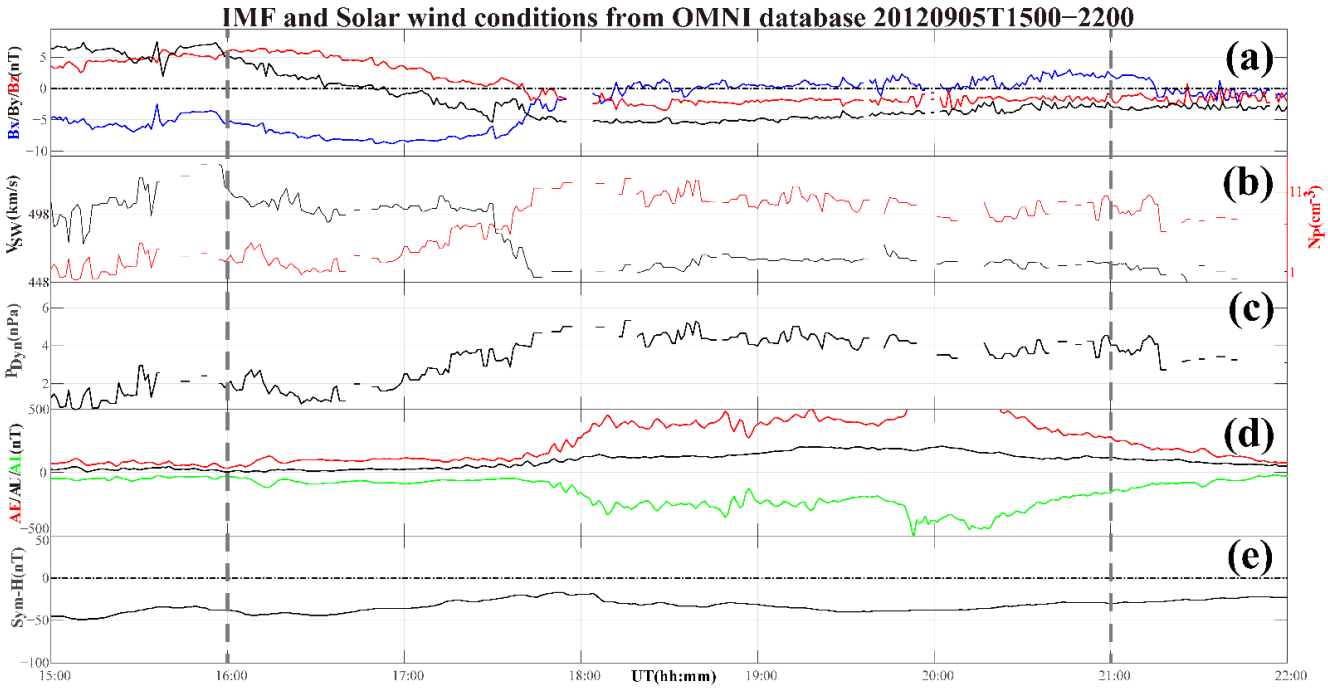

Figure 2. An overview of the solar wind and Interplanetary Magnetic Field (IMF) conditions as well as the geomagnetic indices during a period of 15:00–22:00 UT on 5 September 2012. From top to bottom: (**a**) the IMF Bx (blue), By (black), Bz (red) components; (**b**) the solar wind velocity (black), the solar wind number density (red); (**c**) the solar wind dynamic pressure, PDyn; (**d**) the auroral electrojet (AE/AU/AL) indices; and (**e**) the SYM-H index. Considering the propagation time from the nose of bow shock to the polar ionosphere, the IMF and solar wind data lagged by 7 min. Two vertical dashed lines highlight the conducted period in this study.

3.2. The Characteristics of Polar Cap Es Layer

Figure 3 presents a group range of echoes on 4 MHz from CADI (CADI panel) and electron density profiles along multiple beams of RISR-N (RISR-N panels) at Resolute Bay

(RB) during the interval of 16:00–21:00 UT on 5 September 2012 as a function of UT and altitude [34,35]. A grey dashed vertical line is marked at 16:20 UT on all panels. In the CADI panel, a cloud of echoes (centered at 16:20 UT) rapidly penetrated down to virtual heights below 120 km from up to ~220 km and then disappeared instantly (highlighted by the grey dashed vertical line), which is a clear phenomenon of particle precipitation. Soon after, a clear band of strong echoes (up to 36 dB) emerged and then gently fell from the virtual height of 130 km to 95 km during a long period between 16:30 and 20:50 UT, which are classic signatures of a polar cap Es layer [22]. Above the virtual height of 200 km, a second band of echoes is seen, corresponding to the second hop reflection from the layer. Note that the virtual heights in the CADI panel of Figure 3 are slightly higher than their corresponding real height values.

Moreover, the spatial structures of the polar cap Es layer in 2-dimensions can be examined through the use of Ne profiles from the many phased-array beams of RISR-N. Considering the location of RB (MLT $\approx$ UT$-$7 h), the experiment of interest was happening during daytime conditions, extending from the morning to noon sector. The RISR-N panels in Figure 3 present a number of Ne profiles observed by beams of 8, 3–1, 5–7, and 9–11 during the period of 16:00–21:00 UT on 5 September 2012, which were placed following the column of beams of RISN-N, as shown in Figure 1b (except the noise condition of beam 4 due to the lowest elevation). A color bar is located at the right-side of each panel, all representing the same scale. In the RISR-N panels of Figure 3, there were similar high-density structures rapidly penetrating from >150 km to ~100 km at around 16:20 UT (marked by the grey dashed vertical line), which are considered the particle precipitation and are consistent with the observations in the CADI panel. After this particle precipitation, a clear band with great electron density was seen gradually decreasing in altitude from 110 km to 95 km before dissipating into the background in each RISR-N panel, which almost simultaneously occurred from 16:30 UT to ~20:50 UT. This high Ne in the lower E region is likely the same structure seen in the CADI panel, all highlighting the appearance of the polar cap Es layer. Note that in the beam 3 panel of RISR-N, both the particle precipitation and initial section of the polar cap Es layer were much weaker than in other beams, probably due to its location at the highest MLat. Around 17:50 UT, a second formation of the polar cap Es layer was observed.

Furthermore, noting the period when the polar cap Es layer was observed in all RISR-N beams and taking advantage of the spatial distribution of RISR-N beams, the 2-dimensional scale of polar cap Es layer was roughly estimated (probably >200 km in horizontal), which was calculated at an assumed altitude of 100 km at where it is frequently emerging. Below, the adopted method to roughly estimate the horizontal scale is basically introduced, predominately relying on trigonometric functions. Based on four corner beams of 3, 1, 9, and 11 (Figure 1b), the corresponding intersection points of these beams to the Es layer at the assumed altitude (100 km) were projected to the ground vertically. Then, the horizontal distance from the mapped points to the RISR-N radar (the location of beam 8) was easily calculated by using their elevation angles and the assumed altitude. Lastly, after that the horizontal distances between these four mapped points were simply figured out by referring to their azimuth angles. This horizontal size of the polar cap Es layer was much greater than that of 250 $\times$ 20 km in mid-latitude regions [29,30], probably indicating the different formation mechanisms at high latitudes.

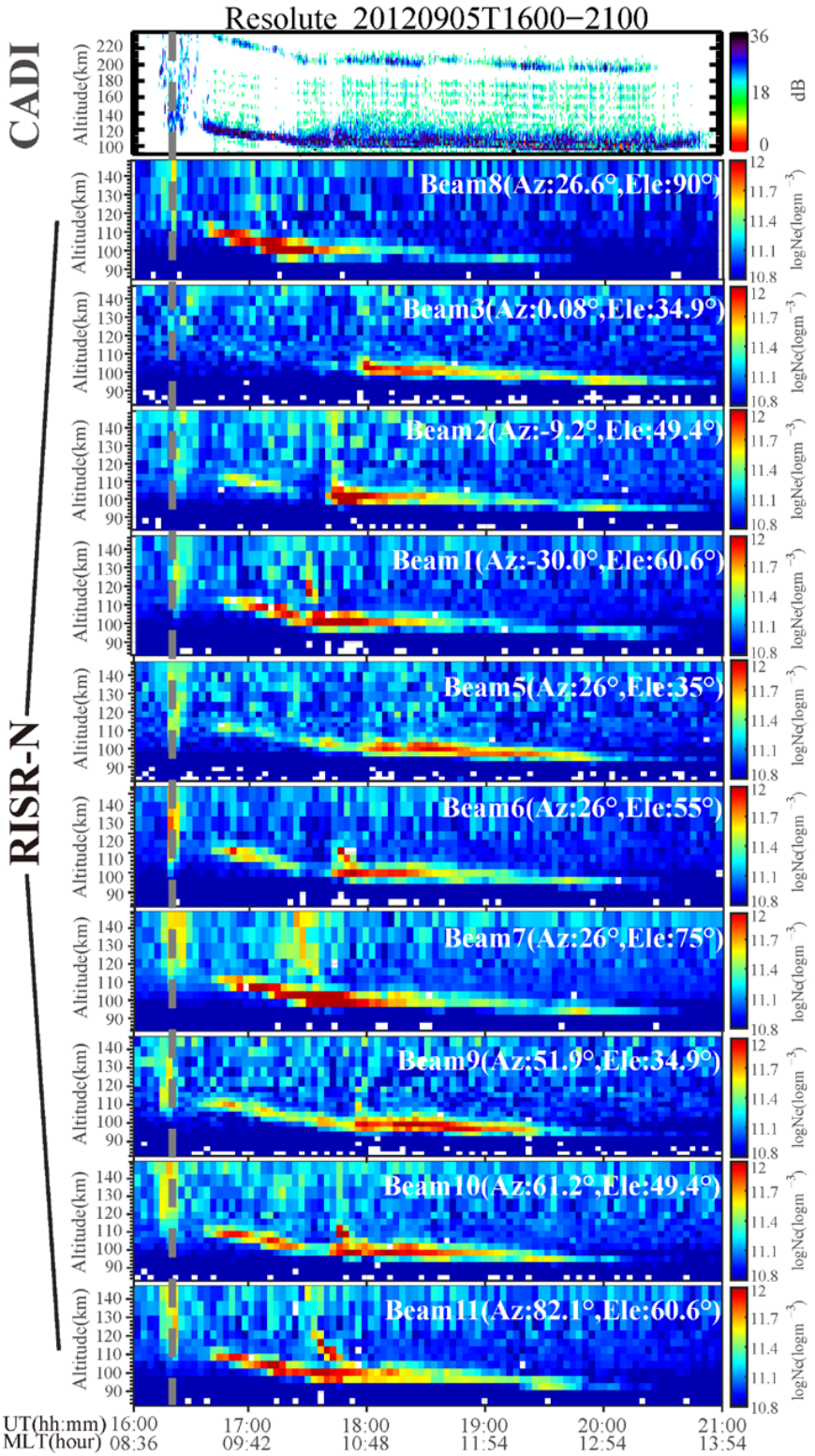

Figure 3. A time series of group range at 4 MHz by CADI (CADI panel) and electron density (Ne) profiles along multiple beams of RISR-N (RISR-N panels) at Resolute Bay (RB) during a time interval of 16:00–21:00 UT on 5 September 2012. The CADI panel possessed a virtual height range of 90–240 km and RISR-N panels employed an altitude range of 80–150 km. At the top-right corner of each RISR-N panel, the numbers of every displayed beam of RISR-N are suggested, together with their elevation and azimuth. A grey dashed vertical line is marked at 16:20 UT.

Additionally, there were three more CADI stations from CHAIN near the RB, providing more evidence to investigate the polar cap Es layer, which was at the EU, PO, and CA. In this experiment, the data from EU and PO were available. Figure 4 shows a group range of echoes on 4 MHz from CADI at Eureka (EU, top) and Pond Inlet (PO, bottom) as a function of UT and virtual height. Similar to the CADI panel of Figure 3 at RB, a clear band of echoes with weaker intensity appeared at the bottom range (~100 km) on both the EU and PO panels of Figure 4, which is the polar cap Es layer. In the EU panel, the polar cap Es layer occurred during the interval of 16:00-21:30 UT (almost interrupted in the interval of 17:30–17:50 UT), which obviously started earlier than in the RB (~16:30 UT). On the contrary, in the PO panel the initial time of the polar cap Es layer (around at 18:00 UT) lagged behind evidently, likely corresponding to the second part of polar cap Es layer in Figure 3 (RB) and also in Figure 4 (EU). In fact, in order to entirely determine the appearance of the polar cap Es layer in this experiment, the ionograms in a cadence of 5 min (not shown here) from these three CADIs (RB, EU, and PO) were also checked, presenting almost the same behaviors of the polar cap Es layer mentioned above.

Then, for the second section of the polar cap Es layer during the time period of 18:00–21:00 UT, these three stations (RB, EU, and PO) observed the polar cap Es layer simultaneously, possibly suggesting the horizontal scale of the polar cap Es layer is much greater than that only from the RB observation. It may be noted that one more key step is needed to completely determining that these three stations capture only one polar cap Es layer at the same time, however, which is beyond the scope of this paper. In the future, an accurate imaging technique in 2-dimensions is still required to solidly investigate the full structure of the polar cap Es layer. Meanwhile, for the first section of the polar cap Es layer during the interval of 16:00–18:00 UT, the appearance of polar cap Es layer was completely different compared with the second section, which was firstly shown in EU and then in RB, but without PO. As a consequence, the different behaviors of these two sections of the polar cap Es layer probably suggest that the generation mechanism to forming these two parts of the polar cap Es layer is possibly different. Regarding the IMF conditions (Figure 2a), their polarities were obviously changing at around 18:00 UT, possibly linking the IMF conditions and the generation of the polar cap Es layer, which requires much more investigations in near future.

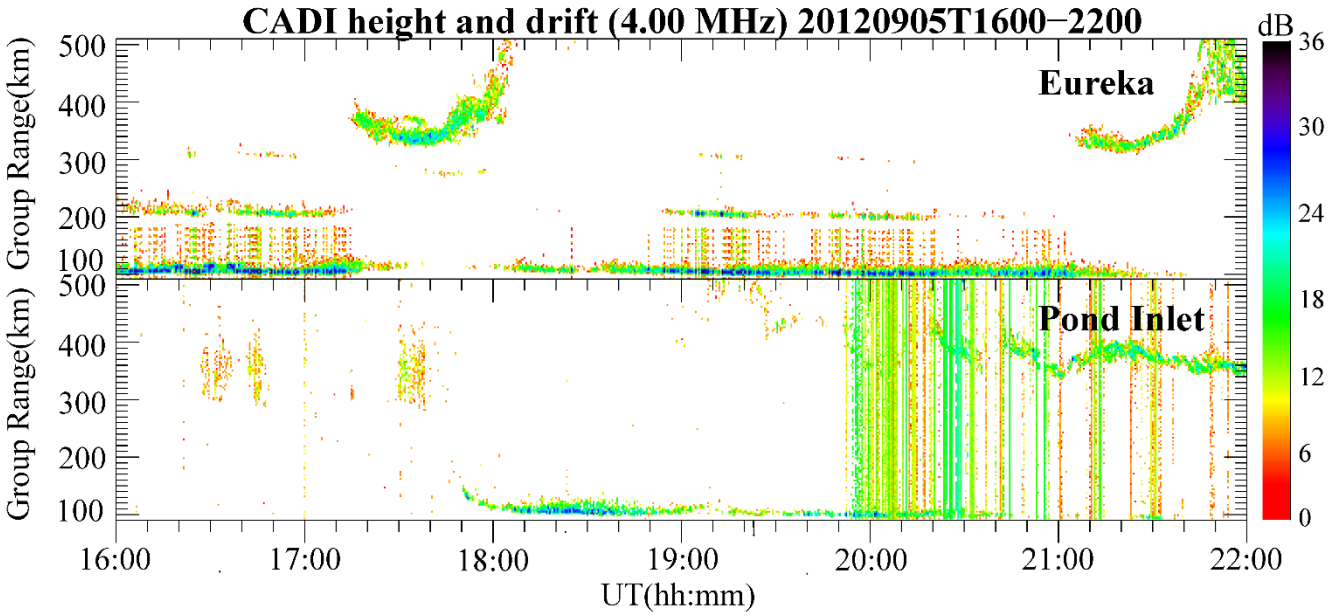

Figure 4. A time series of group range at 4 MHz by CADI (same as the CADI panel of Figure 2) on Eureka (EU, top) and Pond Inlet (PO, bottom) during a time interval of 16:00–22:00 UT on 5 September 2012. These CADI panels possess a virtual height range of 100–500 km.

As mentioned, 11 more RISR-N experiments with the polar cap Es layer were examined which predominately demonstrate similar behavior as this example. In practice, we have carefully checked another example by using RISR-N at RB during a period of 03:00–08:00 UT on 8 August 2012 (not shown here), clearly suggesting the occurrence of polar cap Es layer by almost all beams at the same time. Meanwhile, the group range of echoes at 4 MHz provided by three available CADIs of CHAIN located at RB and CA and PO, respectively, were obviously presenting the appearance of polar cap Es layer. Next, the TEC variations in relation to the polar cap Es layer are investigated in detail.

3.3. TEC Variations

If a ray path from a GPS satellite to a ground-based receiver intersects an Es layer with a smooth F region, the derived GPS TEC will be slightly enhanced, as reported at the mid-latitude region [29–31]. Referring to these published results, at high latitudes the corresponding TEC variations are firstly discussed in the context of both RISR-N- and GPS receiver-derived TEC. The RISR-N TEC roughly estimates the contribution of polar cap Es layer to the GPS receiver-derived TEC of GPS satellite-to-receiver ray. In purpose of exactly comparing the TEC enhancement contributed from the polar cap Es layer provided by RISR-N and GPS receiver in future, the ray path from satellite to GPS receiver should be almost along the line-of-sight of the beams of radar.

Figure 5 shows the time series of RISR-N TEC during the concerned period of 16:30–21:00 UT, 5 September 2012, which were integrated from Ne profiles observed by the beams of 3–1, 5–8, and 9–11 of RISR-N in an altitude range of ~110–95 km corresponding to the altitude of the polar cap Es layer. The red dashed horizontal lines represent 0.5 TECu (1 TECu = 10^{16} electron/m^2). Note that these RISR-N TECs are slant TECs along the corresponding beams under their specific directions. From Figure 5, the RISR-N TEC is found to have a peak value of ~1.7 TECu in beam 7 (but generally ~0.5 TECu). During the specific period of 16:30–20:00 UT that the polar cap Es layer clearly happened, the RISR-N TEC was usually a strong enhancement followed by smaller and rapid variations in Figure 5. Note that the temporal cadence of RISR-N in this experiment was ~3 min, likely requiring much higher time resolution from GPS TEC observations. Close to the end of this period without the clear Es layer (after 20:00 UT), the background of RISR-N TEC within the same altitude range was calculated as <0.1 TECu. Furthermore, the TEC enhancements of the bottom row (at the lowest MLat) of Figure 5 are generally greater than the middle row and then the top (at the highest MLat), except the panels of beams 2 and 7. In addition, regarding the very high peak density of the polar cap Es layer (~$10^{12.1}$ electron/m^3, even greater than the peak of F2 layer) in the beam 7, it is perhaps reasonably surprising that the peak value of TEC enhancement associated with the Es layer in the central polar cap is often lower than 1.7 TECu. In practice, after checking 11 experiments of polar cap Es layers, the normal peak of RISR-N TEC is usually at ~0.5 TECu.

Figure 6 provides a time series of data collected by the ground-based receiver to the GPS PRN19 and GPS PRN18 satellites during a period of 16:00–18:30 UT on 5 September 2012, including (a)/(g) TEC, (b)/(h) TEC variations, (c)/(i) detrended amplitude, and (d)/(j) detrended phase, as well as the calculated (e)/(k) amplitude scintillation indices and (f)/(l) phase scintillation indices. A grey vertical dashed line is located at 16:30 UT. Here, the GPS PRN18 and PRN19 were chosen due to their crossing time coinciding with the emerging period of the polar cap Es layer exactly and the nearest distance of their ray paths to the multiple beams of RISR-N radar simultaneously. In Figure 6a,g, the red solid and black dashed lines respectively represent the slant TEC and the smooth TEC obtained from a moving average method with a time window of 4 min. Here, the smooth method was used to filter out the lower frequency fluctuations of GPS TEC that were possibly generated by larger-scale irregularities. The key parameter of the time window was selected deliberately, not only making the smooth TEC fit the slant TEC precisely, but also featuring the concerned TEC variations apparently. In practice, we have tested a range of time windows from 0.1 min to 20 min to meet the strict criterions. The TEC

variations in Figure 6b,h were derived from subtracting the smooth TEC (black dashed line) to the slant TEC (red solid line). Figure 6c,d,i,j are respectively the detrended amplitude and phase from GPS raw data, which were all calculated by a wavelet method within a cutoff frequency range of 0.19–10.7 Hz [36–38]. Figure 6e,f,k,l are scintillation indices in a cadence of 10 s calculated from the detrended amplitude and phases, respectively, which are discussed in the next section. Note that the trajectories of the GPS PRN19 and PRN18 ray paths in relation to the phased-array beams of RISR-N have been clearly demonstrated in Figure 1b, which were respectively coded by the dark and light blue colors.

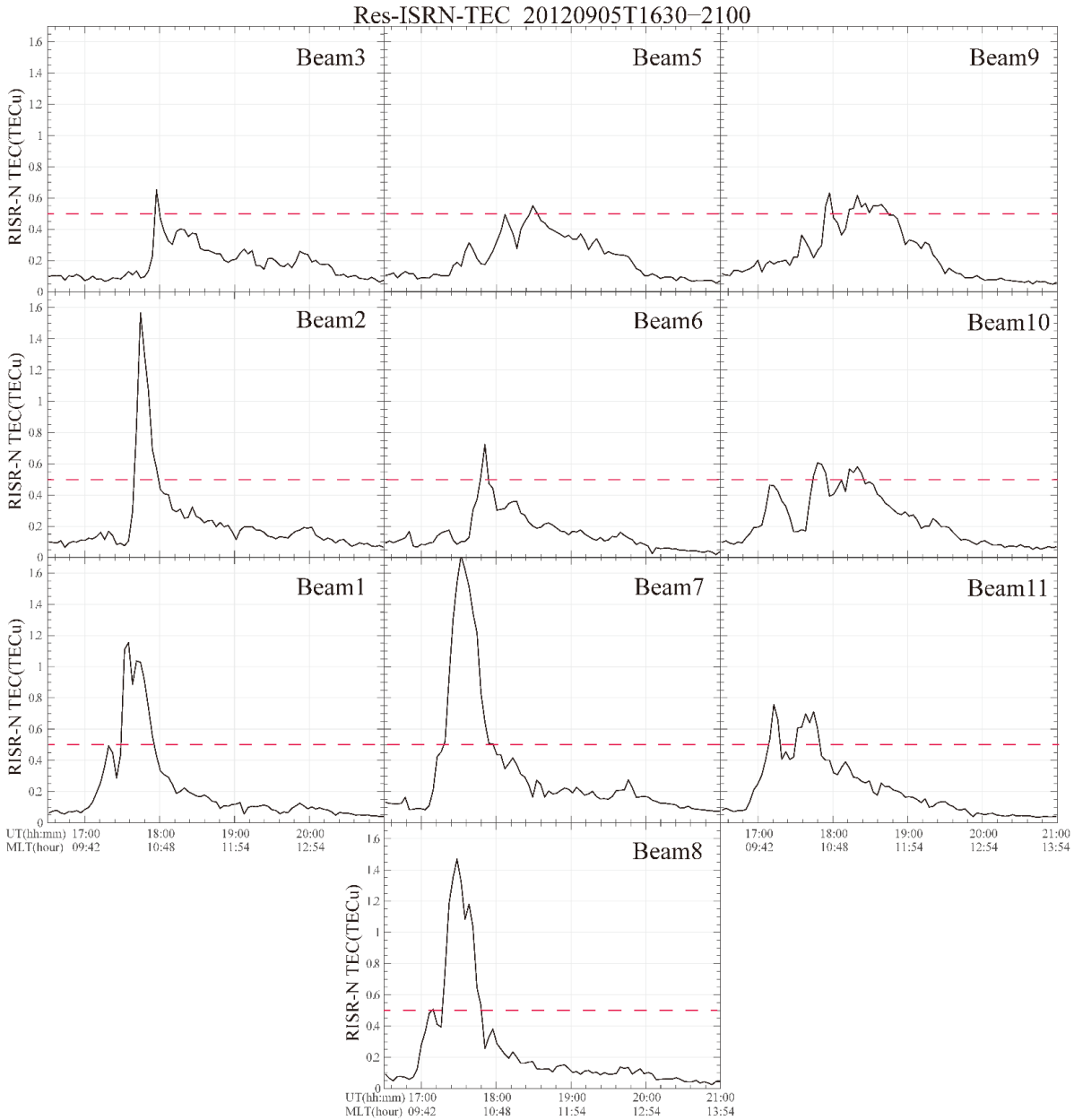

Figure 5. Time series of integrated RISR-N Total Electron Content (TEC) estimated from Ne profiles within the altitudes of the polar cap Es layer (~110 km–95 km) during a period of 16:30–21:00 UT on 5 September 2012, which were placed by beams 3–1, 5–8, and 9–11 of RISR-N. The red horizontal dashed lines highlight 0.5 TECu.

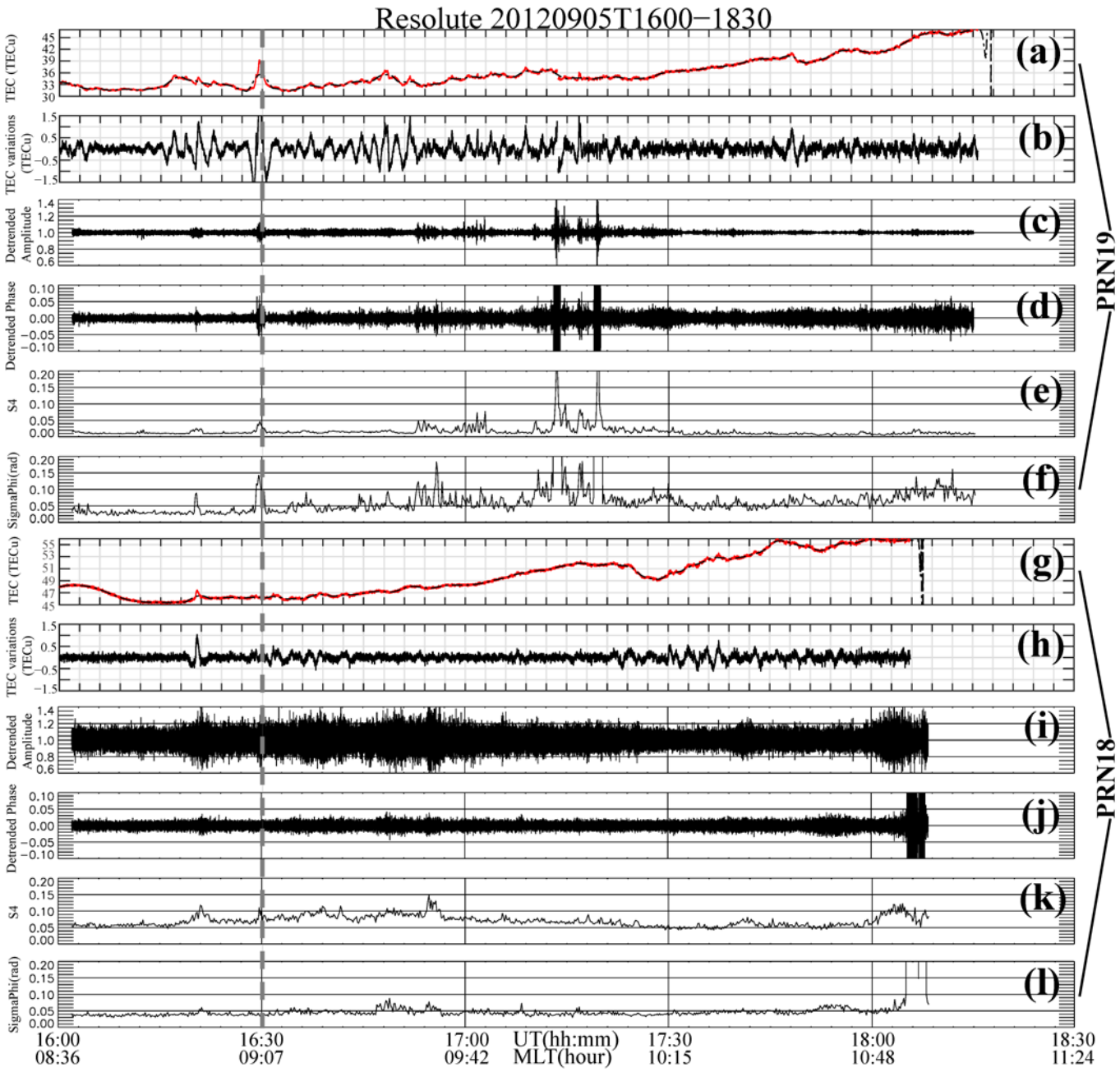

Figure 6. An overview of a large number of parameters obtained from the ground-based GPS receiver at Resolute Bay (RB) to GPS PRN19 (**a**–**f**) and GPS PRN18 (**g**–**l**) during an interval of 16:00–18:30 UT on 5 September 2012. From top to bottom: (**a**/**g**) slant TEC (red solid line), smooth TEC (black dashed line) modelled by a smooth method with a time span of 4 min; (**b**/**h**) TEC variations, subtracting the smooth TEC from the slant TEC; (**c**/**i**) and (**d**/**j**) are the detrended amplitude and detrended phase, which were processed from GPS raw data by the wavelet method; (**e**/**k**) and (**f**/**l**) are the calculated amplitude scintillation indices and phase scintillation indices in a time resolution of 10 s from the detrended raw data. A grey dashed vertical line is highlighted at 16:30 UT.

In Figure 6, at around 16:20 UT (slightly before the grey dashed vertical line), a sharp TEC enhancement is clearly seen at GPS PRN19 (Figure 6a,b) and PRN18 (Figure 6g,h) simultaneously, which corresponds well with the particle precipitation centered at 16:20 UT, as shown in Figure 3 (indicated by the grey dashed vertical line). The TEC variations experienced by GPS PRN19 were stronger than those seen by GPS PRN18, probably due to the stronger part of particle precipitation being encountered by the former. At this moment, the corresponding Ne of beam 11 of RISR-N experienced by GPS PRN19 was

clearly stronger than that in the beam 3 related to GPS PRN18 (Figures 1b and 2). Moreover, from Figure 6c–f,i–l, weak scintillation occurred at this time (~16:20 UT), manifesting as increases in both the amplitude and phase indices of GPS PRN19 and PRN18, which was probably induced by this particle precipitation.

After 16:30 UT (marked by the grey dashed vertical line in Figure 6), the TEC variations are pulse-like enhancements followed by rapid but smaller TEC perturbations with the magnitude around ±0.5 TECu (the maximum amplitude less than 1.8 TECu even at the lower elevation) particularly observed by GPS PRN19 (Figure 6b). Referring to the locations of GPS PRN19 and GPS PRN18 in Figure 1a,b during the whole interval, the TEC variations experienced by GPS PRN19 (Figure 6b) were generally stronger than that by GPS PRN18 (Figure 6h) due to the stronger polar cap Es layers in the lower MLat, which were clearly presented by beams of 1, 7, and 11 of RISR-N in Figures 3 and 5. Furthermore, it is also inferred from that the GPS PRN19 was at a higher elevation than GPS PRN18 and so should have a shorter ray path through the structures. Additionally, comparing the period of 16:30–17:30 UT with the interval after 17:30 UT, the TEC variations by GPS PRN19 in the former period were obviously stronger than in the latter interval (Figure 6b), which also experienced a stronger polar cap Es layer in the lower MLat. These characteristics are consistent with the mentioned point that the level of activity experienced by GPS PRN19 was generally higher than that by GPS PRN18, associated with the intensity distribution of the polar cap Es layer. On the other hand, the assertion is further confirmed by the Rate of TEC (ROT) and ROT Index (ROTI) comparison, which were calculated from the time series of TEC provided by the beam 8 and beam 9 of RISR-N (Figure 5) and GPS PRN19 and PRN18 (Figure 6a,g). Generally speaking, the ROTs from beam 8 and beam 9 of RISR-N were fluctuating between ±0.5 TECu/3 min, which were similar with the ROTs from GPS PRN19 and PRN18. Meanwhile, the ROTIs were also close (almost ~0.15), which presented one more supportive piece of evidence. Consequently, it can be concluded that these TEC variations experienced by GPS PRN19 and also PRN18 were likely induced by the observed polar cap Es layer.

In addition, these pulse-like TEC enhancements (in a time period of ~4 min) are fundamentally different from the platform-like TEC variations created by the polar cap patch (the F region irregularities in [39–41]). Therefore, these long-term pulse-like enhancements, followed by rapid but smaller TEC perturbations, are reasonably linked to the polar cap Es layer rather than the particle precipitation or polar cap patch. Note that the TEC and TEC variations were interrupted at 17:13 UT and 17:19 UT due to cycle slips of the phase of GPS signal, suggesting that propagation conditions may have been particularly troubled during this period plagued by polar cap Es activity.

4. Discussions and Conclusions

In this paper, a case study of polar cap Es layers together with the induced TEC variations and scintillations has been firstly addressed by using combined instruments mainly on Resolute Bay, Eureka, and Pond Inlet, including CADI and multiple beams of RISR-N, as well as a GPS receiver. From these joint observations, the structures of polar cap Es layers were investigated, revealing that the horizontal scale of the polar cap Es layer was extending >200 km, probably due to different formation mechanisms at the mid-latitude region. In order to accurately capture the 2-dimensional structure of the polar cap Es layer and further study the possible mechanisms, the coordinated E region observations of RISR-N and Resolute Bay Incoherent-Scatter Radar-Canada (RISR-C) and CADI all at Resolute, Canada will be carried out soon by taking advantage of 10 more Ne profiles from the twin RISR-C radar, which are looking to the southward directions.

Moreover, the TEC variations caused by the polar cap Es layer have been definitely determined from the RISR-N- and GPS receiver-derived TEC, all following the behavior of a series of pulse-like enhancements (predominately <1.7 TECu, usually ~0.5 TECu) followed by rapid but smaller TEC perturbations. In the future, more experiments of polar cap Es layers are also required to further check our results on the TEC variations.

Furthermore, the corresponding scintillations should be carefully investigated because the scintillations cannot only be used to further understanding the features of plasma irregularities of Es layers in scientific research but can also affect the application of communication/navigations in practice. In this study, from Figure 6c–f on GPS PRN19 and Figure 6i–l on GPS PRN18, after 16:30 UT the scintillation activities of both amplitude and phase became lively, in particular on GPS PRN19, possibly suggesting the capability of the polar cap Es layer to produce scintillations on the L-band signal. Consequently, it reminds us that more attention should be paid to the global Es layer, in particular at mid-latitudes where the Es layer more frequently occurs. However, the difficult point is how to fundamentally separate the scintillation effects produced by the thin polar cap Es layer from the much thicker E/F region plasma irregularities, such as the polar cap patch (or F region irregularities) or particle precipitation. In the near future, much effort is needed to completely decouple it.

Author Contributions: Conceptualization, Y.W., P.T.J.; methodology, D.R.T., A.M.M., Q.-H.Z.; software, R.C.; validation, S.D.; writing—original draft preparation, Y.W.; writing—review and editing, D.R.T., A.M.M.; supervision, P.T.J., Q.-H.Z. All authors have read and agreed to the published version of the manuscript.

Funding: This research in China was funded by the National Natural Science Foundation (grant No. 41574138, 41274149, and 41604139), China Postdoctoral Science Foundation funded project (2020M682163). RISR-N was developed under the NSF cooperative agreement ATM-0121483 to SRI International and the operations and maintenance were supported by NSF cooperative agreement ATM-0608577 to SRI International.

Data Availability Statement: RISR-N data are available at the MIT Haystack Observatory through Madrigal Database (http://cedar.openmadrigal.org/list (accessed on 18 February 2021)). The CADI and GPS data in this work were provided by the Canadian High Arctic Ionospheric Network (CHAIN); the official website is http://chain.physics.unb.ca/chain/ (accessed on 18 February 2021).

Acknowledgments: Infrastructure funding for CHAIN was provided by the Canada Foundation for Innovation (CFI) and the New Brunswick Innovation Foundation (NBIF). CHAIN and its operation are conducted in collaboration with the Canadian Space Agency (CSA). Science funding is provided by the Natural Sciences and Engineering Research Council of Canada (NSERC).

Conflicts of Interest: The authors declare no conflict of interest. The funders had no role in the design of the study; in the collection, analyses, or interpretation of data; in the writing of the manuscript, or in the decision to publish the results.

References

1. Layzer, D. Theory of midlatitude Sporadic E. *Radio Sci.* **1975**, *7*, 385–388. [CrossRef]
2. Narcisi, R.S. Composition studies of the lower thermosphere. In *Physics of Upper Atmosphere*; Royal Society: London, UK, 1971; pp. 12–59.
3. Behnke, R.A.; Vickery, J.F. Radar evidence for Fe^+ in a sporadic-E layer. *Radio Sci.* **1975**, *10*, 325–327. [CrossRef]
4. Turunen, T.; Nygren, T.; Huuskonen, A.; Jalonen, L. Incoherent scatter studies of Sporadic-E using 300 m resolution. *J. Atmos. Terr. Phys.* **1988**, *50*, 277–287. [CrossRef]
5. Shinagawa, H.; Miyoshi, Y.; Jin, H.; Fujiwara, H. Global distribution of neutral wind shear associated with sporadic E layers derived from GAIA. *J. Geophys. Res. Space Phys.* **2017**, *122*, 4450–4465. [CrossRef]
6. Singer, W.; von Zahn, U.; Weiß, J. Diurnal and annual variations of meteor rates at the arctic circle. *Atmos. Chem. Phys.* **2004**, *4*, 1355–1363. [CrossRef]
7. Janches, D.; Palo, S.E.; Lau, E.M.; Avery, S.K.; Avery, J.P.; de la Peña, S.; Makarov, N.A. Diurnal and seasonal variability of the meteoric flux at the South Pole measured with radars. *Geophys. Res. Lett.* **2004**, *31*, L20807. [CrossRef]
8. Kumar, S.; Hanson, W.B. The morphology of metallic ions in the upper atmosphere. *J. Geophys. Res.* **1980**, *85*, 6783–6801. [CrossRef]
9. Bristow, W.A.; Watkins, B.J. Incoherent scatter observations of thin ionization layers at Sondrestrom. *J. Atmos. Terr. Phys.* **1993**, *55*, 873–894. [CrossRef]
10. Yuan, T.; Wang, J.; Cai, X.; Sojka, J.; Rice, D.; Oberheide, J.; Criddle, N. Investigation of the seasonal and local time variations of the high-altitude sporadic Na layer (Na_s) formation and the associated midlatitude descending E layer (E_s) in lower E region. *J. Geophys. Res. Space Phys.* **2014**, *119*, 5985–5999. [CrossRef]

11. Cai, X.G.; Yuan, T.; Vincent Eccles, J.; Raizada, S. Investigation on the distinct nocturnal secondary sodium layer behavior above 95 km in winter and summer over Logan, UT (41.7°N, 112°W) and Arecibo Observatory, PR (18.3°N, 67°W). *J. Geophys. Res. Space Phys.* **2019**, *124*, 9610–9625. [CrossRef]
12. Whitehead, J.D. The formation of the Sporadic-E layer in the temperate zones. *J. Atmos. Terr. Phys.* **1961**, *20*, 49–58. [CrossRef]
13. Carrasco, A.J.; Batista, I.S.; Abdu, M.A. Simulation of the sporadic E layer response to prereversal associated evening vertical electric field enhancement near dip equator. *J. Geophys. Res.* **2007**, *112*, A06324. [CrossRef]
14. Kelley, M.C. *The Earth's Ionosphere: Plasma Physics and Electrodynamics*, 2nd ed.; Elsevier: Cambridge, MA, USA, 2009; pp. 312–335.
15. Haldoupis, C. A tutorial review on sporadic E layers. In *Aeronomy of the Earth's Atmosphere and Ionosphere*; Abdu, M.A., Pancheva, D., Eds.; IAGA Special Sopron Book Series 2; Springer Science+Business Media: Berlin, Germany, 2011. [CrossRef]
16. Yeh, W.H.; Liu, J.Y.; Huang, C.Y.; Chen, S.P. Explanation of the Sporadic-E layer formation by comparing FORMOSAT-3/COSMIC data with meteor and wind shear information. *J. Geophys. Res. Atmos.* **2014**, *119*, 4568–4579. [CrossRef]
17. Nygren, T.; Jalonen, L.; Oksman, J.; Turunen, T. The role of electric field and neutral wind direction in the formation of sporadic E-layers. *J. Atmos. Terr. Phys.* **1984**, *46*, 373–381. [CrossRef]
18. Bristow, W.A.; Watkins, B.J. Numerical simulation of the formation of thin ionization layers at high latitudes. *Geophys. Res. Lett.* **1991**, *18*, 404–407. [CrossRef]
19. Kirkwood, S.; Zhan, U.V. On the role of auroral electric fields in the formation of low altitude sporadic-E and sudden sodium layers. *J. Atmos. Terr. Phys.* **1991**, *53*, 389–407. [CrossRef]
20. Bedey, D.F.; Watkins, B.J. Large-scale transport of metallic ions and the occurrence of thin ion layers in the polar ionosphere. *J. Geophys. Res.* **1997**, *102*, 9675–9681. [CrossRef]
21. Kirkwood, S.; Collis, P. Gravity wave generation of simultaneous auroral sporadic-E layers and sudden neutral sodium layers. *J. Atmos. Terr. Phys.* **1989**, *51*, 259–269. [CrossRef]
22. MacDougall, J.W.; Jayachandran, P.T.; Plane, J.M.C. Polar cap sporadic-E: Part1, observation. *J. Atmos. Terr. Phys.* **2000**, *62*, 1155–1167. [CrossRef]
23. MacDougall, J.W.; Jayachandran, P.T.; Plane, J.M.C. Polar cap sporadic-E: Part2, modelling. *J. Atmos. Terr. Phys.* **2000**, *62*, 1169–1176. [CrossRef]
24. Hines, C.O. Internal atmospheric gravity waves at ionospheric heights. *Can. J. Phys.* **1960**, *38*, 1441–1481. [CrossRef]
25. Axford, W.I. The formation and vertical movement of dense ionized layers in the ionosphere due to neutral wind shears. *J. Geophys. Res.* **1963**, *68*, 769–779. [CrossRef]
26. Fukao, S.; Yamamoto, M.; Tsunoda, R.T.; Hayakawa, H.; Mukai, T. The SEEK (Sporadic-E Experiment over Kyushu) Campaign. *Geophys. Res. Lett.* **1998**, *25*, 1761–1764. [CrossRef]
27. Wu, D.L.; Ao, C.O.; Hajj, G.A.; de la Torre Juarez, M.; Mannucci, A.J. Sporadic E morphology from GPS CHAMP radio occultation. *J. Geophys. Res.* **2005**, *110*, A01306. [CrossRef]
28. Larsen, M.F.; Hysell, D.L.; Zhou, Q.H.; Smith, S.M.; Friedman, J.; Bishop, R.L. Imaging coherent scatter radar, incoherent scatter radar, and optical observations of quasiperiodic structures associated with sporadic E layers. *J. Geophys. Res.* **2007**, *112*, A06321. [CrossRef]
29. Maeda, J.; Heki, K. Two-dimensional observations of midlatitude sporadic E irregularities with a dense GPS array in Japan. *Radio Sci.* **2014**, *49*, 28–35. [CrossRef]
30. Maeda, J.; Suzuki, T.; Furuya, M.; Heki, K. Imaging the midlatitude sporadic E plasma patches with a coordinated observation of spaceborne InSAR and GPS total electron content. *Geophys. Res. Lett.* **2016**, *43*, 1419–1425. [CrossRef]
31. Sun, W.J.; Ning, B.Q.; Yue, X.A.; Li, G.Z.; Hu, L.H.; Chang, S.M.; Lan, J.P.; Zhu, Z.P.; Zhao, B.Q.; Lin, J. Strong sporadic E occurrence detected by ground-based GNSS. *J. Geophys. Res. Space Phys.* **2018**, *123*, 3050–3062. [CrossRef]
32. Jayachandran, P.T.; Langley, R.B.; MacDougall, J.W.; Mushini, S.C.; Pokhotelov, D.; Hazma, A.M.; Mann, I.R.; Milling, D.K.; Kale, Z.C.; Chadwick, R.; et al. Canadian High Arctic Ionospheric Network (CHAIN). *Radio Sci.* **2009**, *44*, RS0A03. [CrossRef]
33. Bahcivan, H.; Tsunoda, R.; Nicolls, M.; Heinselman, C. Initial ionospheric observations made by the new Resolute incoherent scatter radar and comparison to solar wind IMF. *Geophys. Res. Lett.* **2010**, *37*, L15103. [CrossRef]
34. Haldoupis, C.; Meek, C.; Christakis, N.; Pancheva, D.; Bourdillon, A. Ionogram height-time-intensity observations of descending sporadic E layers at mid-latitude. *J. Atmos. Sol. Terr. Phys.* **2006**, *68*, 539–557. [CrossRef]
35. Pignalberi, A.; Pezzopane, M.; Zuccheretti, E. Sporadic E layer at mid-latitudes: Average properties and influence of atmospheric tides. *Ann. Geophys.* **2014**, *32*, 1427–1440. [CrossRef]
36. Mushini, S.C.; Jayachandran, P.T.; Langley, R.B.; MacDougall, J.W.; Pokhotelov, D. Improved amplitude- and phase-scintillation indices derived from wavelet detrended high-latitude GPS data. *GPS Solut.* **2012**, *16*, 363–373. [CrossRef]
37. McCaffrey, A.M.; Jayachandran, P.T. Spectral characteristics of auroral region scintillation using 100 Hz sampling. *GPS Solut.* **2017**. [CrossRef]
38. McCaffrey, A.M.; Jayachandran, P.T. Determination of the refractive contribution to GPS phase "scintillation". *J. Geophys. Res. Space Phys.* **2019**, *124*, 1454–1469. [CrossRef]
39. Krankowaki, A.; Shagimuratov, I.I.; Baran, L.W.; Ephishov, I.I.; Tepenitzyna, N.J. The occurrence of polar cap patches in TEC fluctuations detected using GPS measurements in southern hemisphere. *Adv. Space Res.* **2006**, *38*, 2601–2609. [CrossRef]

40. Zhang, Q.H.; Zong, Q.G.; Lockwood, M.; Heelis, R.A.; Hairston, M.; Liang, J.; McCrea, I.; Zhang, B.C.; Moen, J.; Zhang, S.R.; et al. Earth's ion upflow associated with polar cap patches: Global and in situ observations. *Geophys. Res. Lett.* **2016**, *43*, 1845–1853. [CrossRef]
41. Jin, Y.Q.; Moen, J.; Oksavik, K.; Spicher, A.; Clausen, B.N.; Miloch, W.J. GPS scintillations associated with cusp dynamics and polar cap patches. *J. Space Weather Space Clim.* **2017**, *7*, A23. [CrossRef]